AGU ADVANCING EARTH AND SPACE SCIENCE

Geophysical Research Letters

RESEARCH LETTER
10.1029/2022GL101256

Key Points:

- A new model of seismic shear-wave velocity beneath Alaska was obtained by jointly inverting surface wave and Sp body wave data
- The Denali fault lies just south of the margin of thicker and higher velocity upper plate lithosphere, as does the Kobuk fault
- These results support the view that gradients in lithospheric strength can be key to the localization of major continental strike-slip faults

Supporting Information:

Supporting Information may be found in the online version of this article.

Correspondence to:

I. Gama,
isabellagamad@gmail.com

Citation:

Gama, I., Fischer, K. M., Dalton, C. A., & Eilon, Z. (2022). Variations in lithospheric thickness across the Denali fault and in Northern Alaska. *Geophysical Research Letters*, *49*, e2022GL101256. https://doi.org/10.1029/2022GL101256

Received 13 SEP 2022
Accepted 11 DEC 2022

Author Contributions:

Conceptualization: Isabella Gama, Karen M. Fischer
Data curation: Isabella Gama
Formal analysis: Isabella Gama
Funding acquisition: Karen M. Fischer, Colleen A. Dalton
Investigation: Isabella Gama
Methodology: Isabella Gama, Karen M. Fischer, Zachary Eilon
Project Administration: Karen M. Fischer, Colleen A. Dalton
Resources: Isabella Gama, Karen M. Fischer, Colleen A. Dalton, Zachary Eilon
Software: Isabella Gama, Zachary Eilon
Supervision: Karen M. Fischer

Variations in Lithospheric Thickness Across the Denali Fault and in Northern Alaska

Isabella Gama[1], Karen M. Fischer[1], Colleen A. Dalton[1], and Zachary Eilon[2]

[1]Department of Earth, Environmental and Planetary Sciences, Brown University, Providence, RI, USA, [2]Department of Earth Sciences, University of California, Santa Barbara, CA, USA

Abstract While variations in crustal structure beneath the Denali fault in Alaska are well-documented, the existence of fault-correlated structures throughout the entire thickness of the continental lithosphere is not. A new model of shear-wave velocity structure obtained through joint inversion of surface wave and converted body wave data shows a northward increase in lithospheric thickness and velocity occurring across the Denali fault system. In northern Alaska, a dramatic increase in lithospheric thickness at the southern margin of the Arctic-Alaska terrane lies in the vicinity of the Kobuk fault system. These correlations support the view that transpressive deformation tends to localize at the margins of thicker, higher-strength lithosphere.

Plain Language Summary Major faults in Earth's tectonic plates, such as Alaska's Denali fault, begin as brittle fractures of the shallow crust and progress to include ductile shearing of the deeper crust. Changes in tectonic plate thickness or internal temperature have been observed beneath some faults, consistent with feedback between the strength of the deeper plate and the location of the fault. Using global earthquake signals, we built a new 3-D model of seismic velocity structure throughout Alaska, extending from the surface to hundreds of kilometers in depth. According to the model, the Denali fault coincides with a northward thickening and an apparent abrupt temperature increase within Alaska's plate. Further north, at another boundary between geological provinces near the Kobuk fault, we also find an abrupt thickening of the plate. These relationships are consistent with faults being located near the edges of thicker, stronger regions of the tectonic plates.

1. Introduction

Globally, prior work has shown that several continental strike-slip faults are connected to shear zones in the mantle with distinct signatures. These signatures include mantle deformation fabrics (e.g., Bürgmann & Dresen, 2008; Cao & Neubauer, 2016; Norris & Toy, 2014; Teyssier & Tikoff, 1998; Titus et al., 2007; Vauchez et al., 2012), or changes in lithospheric thickness and mantle velocity gradients that are inferred to span the entire thickness of the lithosphere (e.g., the Altyn Tagh fault, Wittlinger et al., 1998; the Tanlu fault zone, Chen et al., 2006; the Northern Anatolian fault, Fichtner et al., 2013; the central San Andreas Fault, Ford et al., 2014; the Moroccan Atlas fault, Miller & Becker, 2014; the Alpine Fault, Hua et al., 2018; the Tintina fault, Estève et al., 2020). In Alaska, the Denali fault (Figure 1b) is a remarkable strike-slip system extending over 2,000 km in length. It has been active since at least 65 Ma, has accommodated hundreds of kilometers of dextral motion, and has maintained a relatively stable curvature since 45 Ma (Benowitz et al., 2022; Regan et al., 2020). The Denali fault also plays a fundamental role in the mechanics of how shortening due to subduction in southern Alaska is partitioned into upper plate deformation (e.g., Jadamec et al., 2013). However, while abundant evidence exists for offsets in crustal thickness and velocity across the Denali fault and the adjacent Hines Creek fault (Allam et al., 2017; Brennan et al., 2011; Gama et al., 2022; Haney et al., 2020; Mann et al., 2022; Martin-Short et al., 2018; Miller, O'Driscoll, et al., 2018; Miller, Roeske, & Benowitz, 2018; Rossi et al., 2006; Veenstra et al., 2006; Ward, 2015) the connection of the Denali fault to structures in the deeper mantle lithosphere has remained uncertain. In a new model of shear-wave velocity structure obtained from joint inversion of surface wave and converted body wave data, we find that the Denali fault lies above a transition in lithospheric thickness. We also find that the Kobuk fault, a now low-slip dextral strike-slip fault in the southern foothills of the Brooks Range in northern Alaska (Avé Lallement et al., 1998; Elliott & Freymueller, 2020), lies close to a dramatic northward increase in lithospheric thickness.

Validation: Isabella Gama, Colleen A. Dalton
Visualization: Isabella Gama
Writing – original draft: Isabella Gama
Writing – review & editing: Isabella Gama, Karen M. Fischer, Colleen A. Dalton, Zachary Eilon

2. Joint Inversion of Rayleigh Wave Phase Velocities and a Sp Receiver Function Stack

We obtained new constraints on the crust and mantle shear wave velocity structure beneath Alaska through joint inversion of two complementary data types: (a) fundamental mode Rayleigh wave phase velocities, which provide information on absolute shear velocities as a function of depth and (b) a stack of S-to-P (Sp) converted waves, which enhance the resolution of vertically-localized velocity gradients such as the Moho and lithosphere-asthenosphere boundary (Eilon et al., 2018; Gama et al., 2021).

Sp information was derived from a common conversion point (CCP) stack of Sp receiver functions (Gama et al., 2022) based on 449 broadband stations in Alaska (Figure 1a) (network information provided in the Data Availability Statement section), including 153 stations of the NSF EarthScope Transportable Array. For earthquakes larger than Mw 5.8, recorded between 1986 and 2021, 73,500 Sp receiver functions were calculated from waveforms filtered with a 2–100 s bandpass. The receiver functions were projected to a 3D volume using Fresnel-zone-based weighting functions (Hua, Fischer, Wu, & Blom, 2020) and the velocity model of Nayak et al. (2020).

Fundamental-mode Rayleigh-wave phase velocities for broadband stations in Alaska, including EarthScope Transportable Array stations, were obtained from ambient noise and earthquake sources (Figure S1 of Supporting Information S1). For Rayleigh waves generated by earthquakes, we followed the approach of Babikoff and Dalton (2019) to calculate phase velocities at periods 30–140 s. Ambient noise phase velocities for periods from 5 to 25 s, were obtained using the method of Ekström et al. (2009). More description of these analyses appears in the Supporting Information.

The surface and converted wave data were jointly inverted using a transdimensional hierarchical Bayesian approach (explained in more detail in Eilon et al., 2018 and Gama et al., 2021) in 444 1-D vertical columns (Figure 2d) regularly spaced at 0.5° in latitude and 1.0° in longitude, except where gaps in data necessitated a sparser grid. Shear-wave velocity (Vs) was parameterized using adaptive cubic B-spline functions in the crust and mantle, where the number and depth of the spline knots were allowed to vary as required by the data. Other parameters include the depth and velocity contrast at the Moho, a single ratio of compressional-wave velocity (Vp) to Vs in the crust, and hyperparameters that describe the relative uncertainties of the two data types. Vp/Vs in the mantle was assumed from the AK135 reference model (Kennett et al., 1995), and density was obtained from the Vs-density scalings of Brocher (2005) for the crust and Abers and Hacker (2016) for the mantle. Tests of this inversion approach with synthetic Rayleigh wave phase velocities and Sp receiver functions demonstrate that it is effective at resolving Vs as a function of depth, including vertically-localized gradients (Gama et al., 2021).

For each iteration in six parallel chains of 20,000 iterations we a) generated a synthetic Earth velocity profile by randomly perturbing individual model parameters using the ranges and probabilities shown in Table S1 of Supporting Information S1, b) forward-calculated the corresponding Sp receiver function and Rayleigh wave dispersion curve predictions, c) calculated the misfits of these predictions to the observed Sp CCP stack and Rayleigh wave phase velocities, and d) accepted or rejected each model based on its posterior probability. Predicted Sp receiver functions were obtained from synthetic waveforms calculated with a propagator matrix method (Keith & Crampin, 1977) using the same processing that was applied to the real Sp data prior to CCP stacking. For the body-wave data, misfit was defined as the difference between the convolution of the observed receiver function stack with the synthetic parent phase and the convolution of the synthetic receiver function with the Gaussian function used in the deconvolution (half-width of 0.9 s). This approach accounts for differences in the frequency content of observed and predicted receiver functions. Predicted fundamental-mode Rayleigh wave phase velocities were obtained using Fréchet kernels, with eigenfunctions calculated by Mineos (Masters et al., 2011). Misfit for surface wave data was based on the difference between predicted and observed phase velocities. We accepted or rejected the model from each iteration by applying a Metropolis-Hastings acceptance criterion (Hastings, 1970) to the posterior probability calculated with the prior and likelihood functions, following the approach in Eilon et al. (2018) and Gama et al. (2021). The prior distributions for all parameters were determined empirically (Eilon et al., 2018), were roughly uniform, and were constrained by the bounds in Table S1 of Supporting Information S1.

To form a final model probability distribution, we combined the posterior distributions of all accepted chains, excluding "burn in" models in the first eight thousand iterations when model distributions have sometimes not

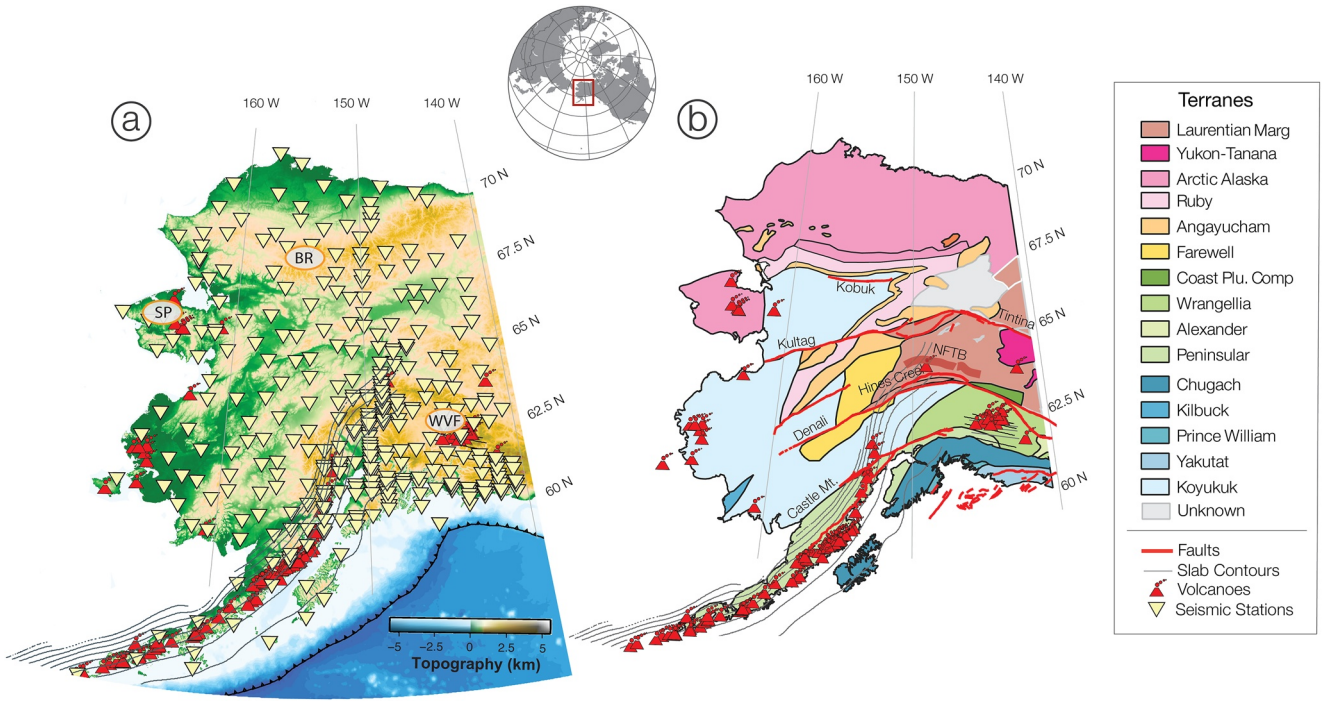

Figure 1. Study region. (a) The 449 broadband seismic stations used in this study (yellow inverted triangles) superimposed on topography (ETOPO1, Amante & Eakins, 2009). Red triangles are Quaternary volcanoes (avo.alaska.edu) and gray lines are slab contours (Daly et al., 2021; Hayes et al., 2018). BR: Brooks Range; SP: Seward Peninsula; WVF: Wrangell Volcanic Field. (b) Major faults (thick red lines) from Elliott and Freymueller (2020), except for the Hines Creek Fault and the Northern Foothills Thrust Belt (NFTB) which are from Benowitz et al. (2022), superimposed on tectonic terranes (Colpron et al., 2007; Colpron & Nelson, 2011).

achieved stationarity and are not representative of the global data misfit minimum. The final Vs model was defined by the median Vs of the ensemble at each depth. Vs uncertainty was described by the 68th percentile range of values at each depth (Figure S2 of Supporting Information S1). Examples of Vs versus depth obtained through the individual 1D inversions are shown in Figure S3 and Figure S4 of Supporting Information S1.

3. Results and Discussion

3.1. Shear Wave Velocity Structure Beneath Alaska: Large-Scale Patterns

At a depth of 44 km, the Vs model contains significant gradients across the Denali fault (Figure 2a). Velocities are typically greater than 4.4 km/s to the north of the Denali fault, corresponding to mantle lithosphere, whereas velocities range from 4.0 to 4.3 km/s to the south, corresponding to a combination of thick crust and low velocity asthenospheric mantle. The magnitude of this velocity contrast is significant in comparison to the 68th percentile (one-standard-deviation) velocity uncertainties, which are less than 0.05 km/s over most of this region (Figure S2a of Supporting Information S1). A band of lower velocities also occurs beneath the Brooks Range in the northern Arctic Alaska terrane (Figure 2a) where thicker crust exists (e.g., Gama et al., 2022; Haney et al., 2020; Miller, O'Driscoll, et al., 2018; Miller, Roeske, & Benowitz, 2018; Zhang et al., 2019).

At a depth of 100 km, a significantly higher Vs mantle, corresponding to the thick lithosphere, is found beneath the northern Arctic Alaska terrane, in contrast to the lower velocities that characterize the central latitudes to the south (Figure 2b). Even further south, velocity variations are dominated by high velocities surrounding the zone of subducting lithosphere (e.g., around the contours marking the top of the slab in Figures 2b and 2c), with lower velocities in adjacent regions that are presumably asthenosphere. At 100 km, Vs is particularly low to the northeast of the Wrangell Volcanic Field, and beneath southwest Alaska and the Seward Peninsula. At 160 km (Figure 2c), the localized lowest velocities in eastern Alaska have shifted to a position directly beneath the Wrangell Volcanic Field, and the highest velocity regions in northern Alaska have expanded southward of the margin of the northern Arctic Alaska terrane. Additional Vs maps appear in Figure S5 of Supporting Information S1.

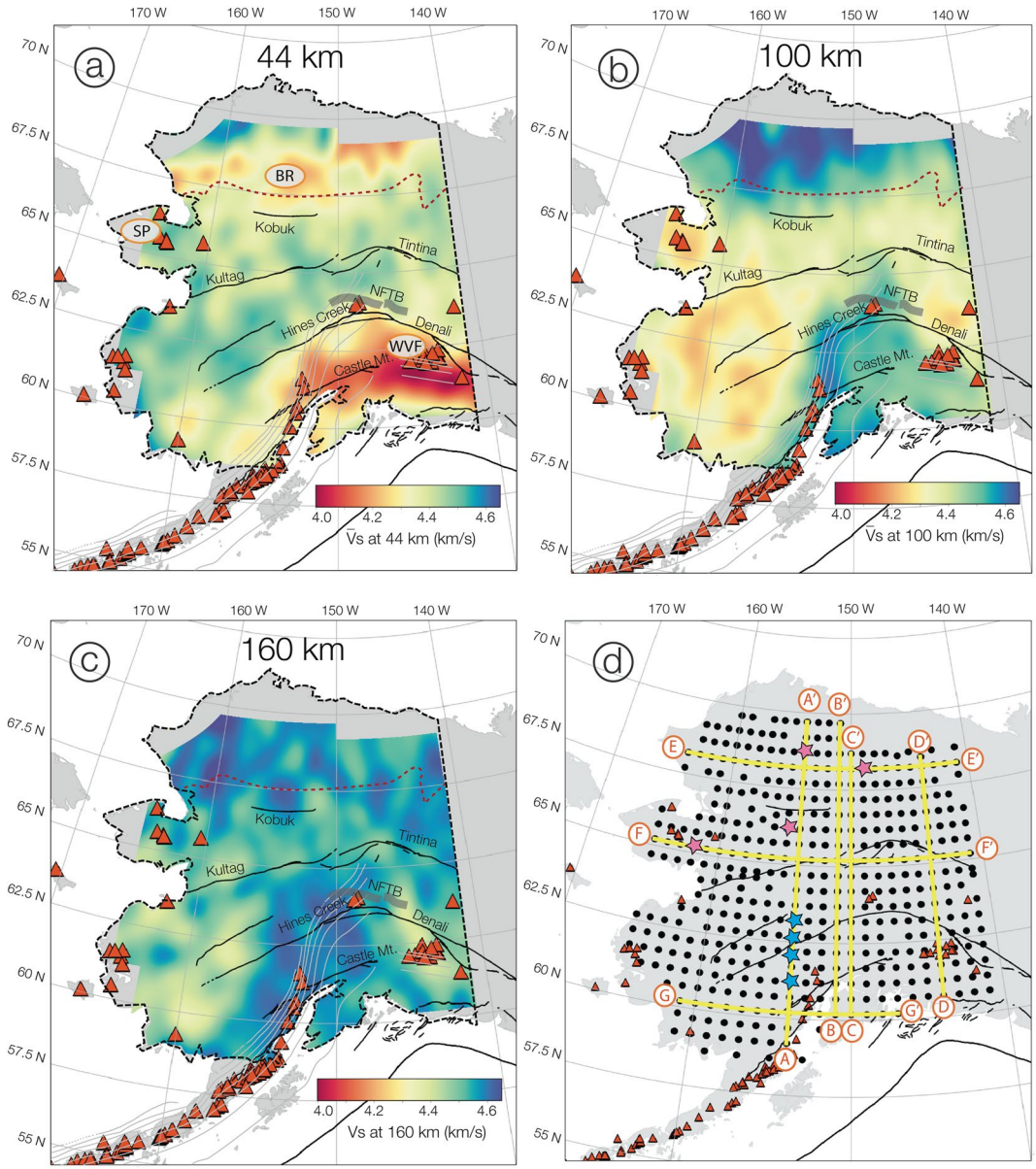

Figure 2. Shear-wave velocity (Vs) at depths of (a) 44 km, (b) 100 km, and (c) 160 km interpolated from the individual Vs models from the joint inversions. Dark red dashed line marks the southern boundary of the northern Arctic Alaska terrane (Colpron & Nelson, 2011). (d) Map of locations of the 444 1D inversions. Figures 3 and 4 cross-sections are shown in yellow. Locations of models in Figure S3 of Supporting Information S1 are shown by pink stars and those in Figure S4 of Supporting Information S1 by blue stars. Faults (black and gray lines), volcanoes, and slab contours cited in Figure 1. BR: Brooks Range; SP: Seward Peninsula; WVF: Wrangell Volcanic Field.

At a broad-scale, cross-sections through the Vs model are dominated by the subduction-related structures in the south and thick lithosphere in northernmost Alaska. A clear low Vs asthenosphere at depths of 50–150 km extends to the north and west over distances of more than 750 km away from the subducting lithosphere as indicated by seismicity (Figure 3 and cross-section G in Figure 4). On N-S profiles (Figure 3), this low velocity asthenosphere terminates where it meets the thick lithosphere beneath the northern Arctic Alaska terrane. Zones of high velocity surround the dipping seismicity associated with the subducting Pacific lithosphere (cross-sections A, B, C and G), and a high velocity anomaly is co-located with the dipping seismicity found by Daly et al. (2021) beneath the Wrangell Volcanic Field (cross-section D), similar to the high velocity features resolved by Berg et al. (2020), Yang and Gao (2020), and Estève et al. (2021). However, the Rayleigh wave phase velocities and Sp receiver

10.1029/2022GL101256

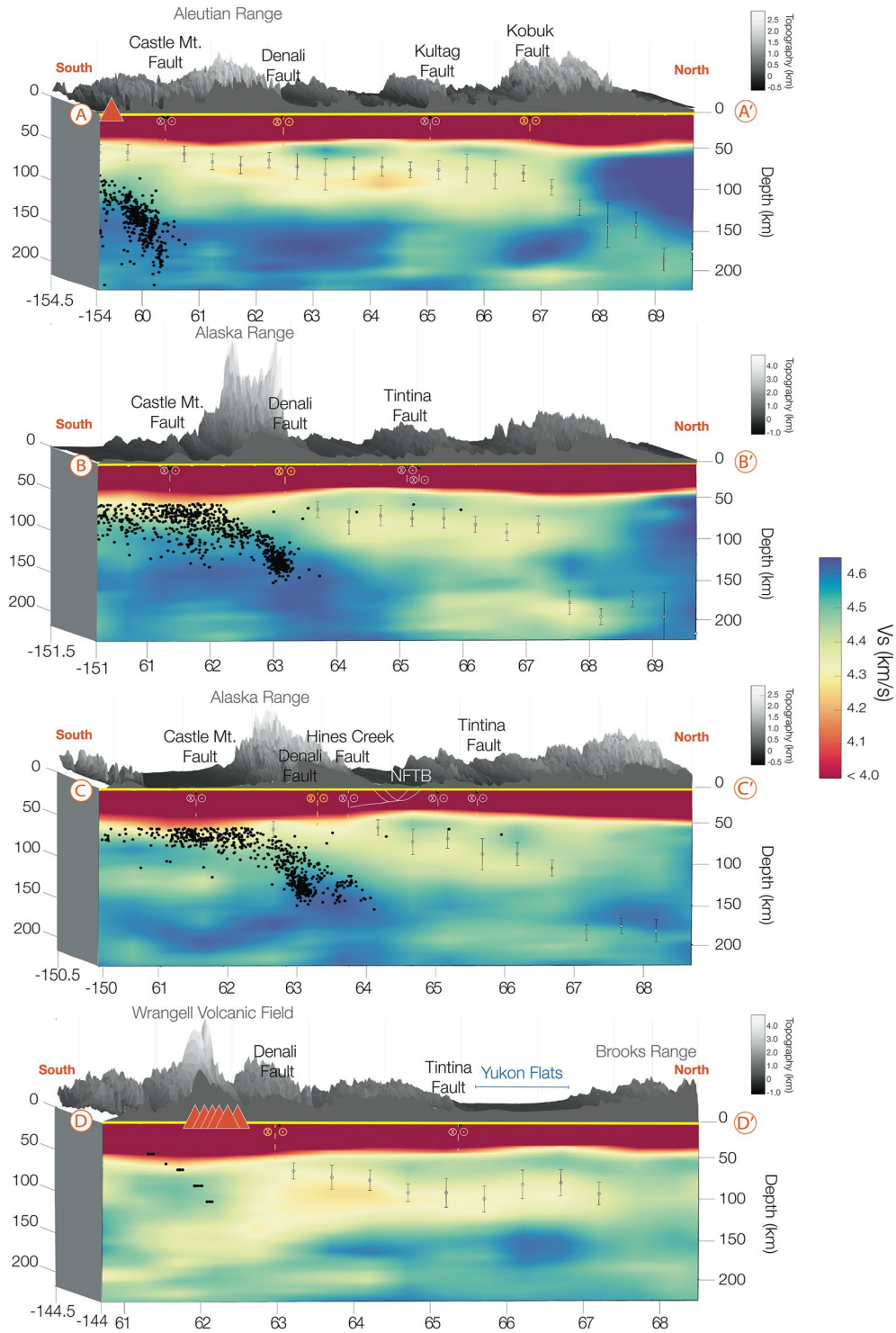

Figure 3. Vs cross-sections (oriented S-N). Topography from ETOPO (Amante & Eakins, 2009) shown in gray. Red triangles are volcanoes and black dots are seismicity within 50 km of the cross-section. In profile D-D', black dots are Wrangell slab contours (Daly et al., 2021) within 20 km. Dashed vertical lines are major strike-slip faults; Denali and Kobuk faults are in yellow; NFTB labeled in (c). White dots with error bars are upper plate lithospheric thicknesses (Supporting Information).

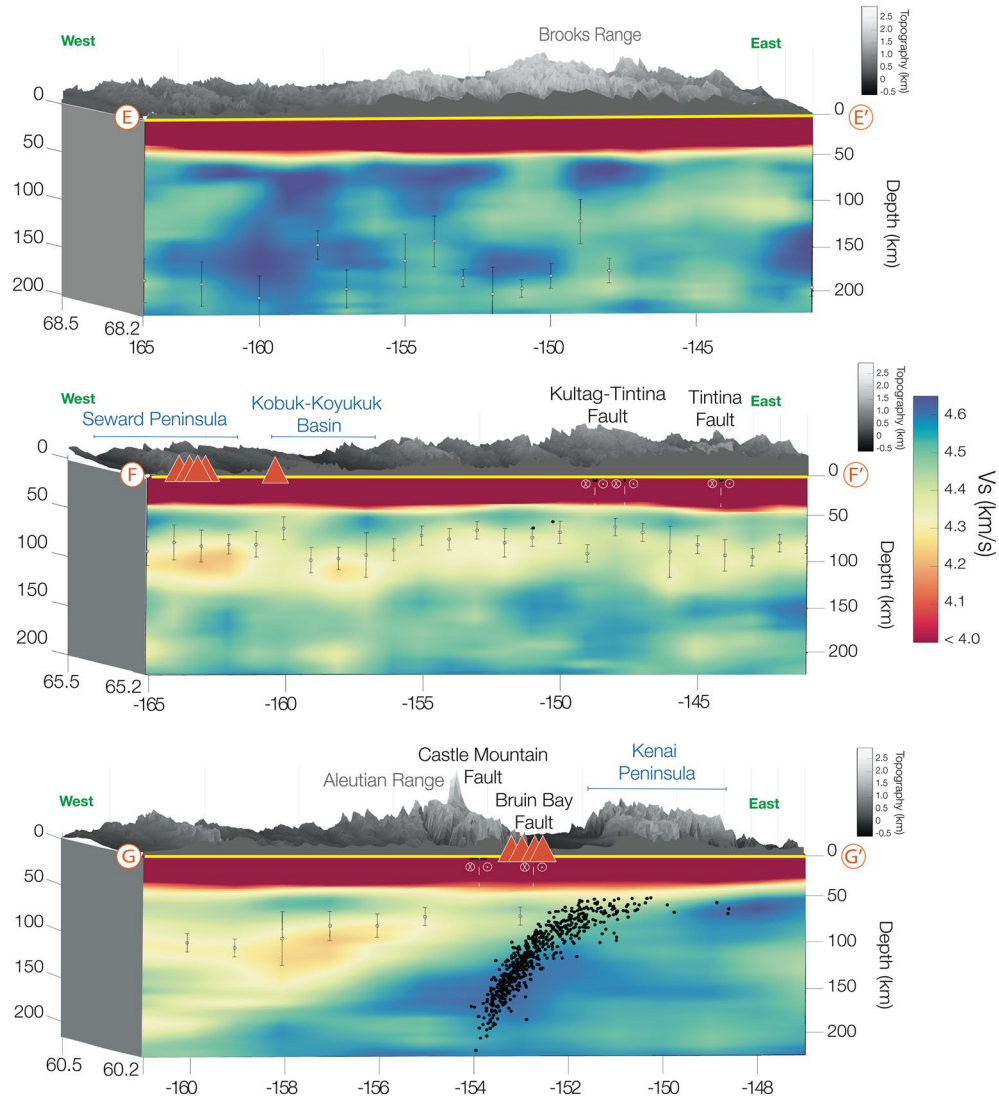

Figure 4. Vs cross-sections (oriented W-E). Topography, volcanoes, seismicity and strike-slip faults as in Figure 3. White dots with error bars are upper plate lithospheric thicknesses; values in northern Alaska (profile E) should be interpreted with care (Supporting Information).

function stacks employed in the inversions for Vs are not ideal for resolving relatively narrow dipping structures (e.g., Hansen & Schmandt, 2017; Hua, Fischer, Mancinelli, & Bao, 2020) and the shapes of these slab-associated high velocity anomalies should not be over-interpreted. On cross-sections C (Figure 3) and G (Figure 4), an asthenospheric low velocity zone with a smaller velocity reduction appears beneath the subducting lithosphere. The Vs model contains a localized region of particularly low asthenospheric velocities beneath the Seward Peninsula, consistent with the Vs models of Berg et al. (2020) and Gama et al. (2021), and with potential mantle upwelling suggested by magmas formed by decompression melting on the Seward Peninsula (Andronikov & Mukasa, 2010; Mukasa et al., 2007).

3.2. Offsets in Lithospheric Thickness Across the Denali Fault

The prominent south-to-north increase in shallow Vs across the Denali fault system (seen at 44 km depth in Figure 2a) reflects a gradient in the thickness and velocity of the mantle lithosphere, as well as crustal structure. For example, as shown in cross-section A (Figure 3), the Denali fault lies at the southern edge of the upper plate lithosphere that is thicker (>65 km) and has a significantly higher velocity than the lithosphere to the south (See

Supporting Information for lithospheric thickness estimation). This gradient is also seen in the individual Vs versus depth models obtained from the inversions (Figure S4 of Supporting Information S1). Elsewhere, the Denali fault is located at the southern edge of thicker and higher Vs upper plate lithosphere (cross-section B in Figure 3) or at the toe of a wedge of higher Vs upper plate mantle (cross-section D in Figure 3). As the exception that proves the rule, the central segment of the Denali fault (cross-section C in Figure 3) lies south of the southern margin of thickening upper plate lithosphere. However, at this longitude, active deformation continues further north, both on the transpressive Hines Creek fault system and the Northern Foothills Thrust Belt, as inferred by Benowitz et al. (2022) (Figures 1b and 3c), reaching the latitude where the upper plate thickens and mantle velocities increase to ~4.5 km/s. Possible reductions in upper plate thickness associated with other major strike-slip faults also appear in the Vs model, for example, at the Kultag and Kobuk faults in cross-section A (Figure 3). However, unlike the Denali fault, these spatial relationships are not consistently observed along fault strikes.

The horizontal resolution of Vs in the model is sufficient to capture variations across major fault systems. For example, the gradients in lithospheric thickness and velocity across the Denali and Hines Creek faults on cross-sections A-D (Figure 3) are resolved at scales of ~60 km. Resolution is determined by the spacing of the individual 1D inversions for Vs (50–55 km), and the lateral resolution of the Rayleigh wave phase velocities; at the periods that are most sensitive to depths of 40–60 km, the latter is on the order of 60 km where station spacing is 60 km or less (as it is across the Denali fault on cross-sections A-D), and at the scale of station spacing elsewhere. Sp phases from 40 to 60 km depths can resolve lateral variations at scales of ~60 km, or even less (Lekic et al., 2011; Lekic & Fischer, 2017).

The observed variations in the thickness and velocity of the upper plate mantle lithosphere across the Denali fault and Hines Creek fault/Northern Foothills Thrust Belt are spatially correlated (at distances of <50 km) with the -changes in Moho depth and velocity across these faults found in prior studies (Allam et al., 2017; Brennan et al., 2011; Gama et al., 2022; Haney et al., 2020; Mann et al., 2022; Martin-Short et al., 2018; Miller, O'Driscoll, et al., 2018; Rossi et al., 2006; Veenstra et al., 2006; Ward, 2015). In addition, the northward decrease in crustal thickness noted at the Hines Creek Fault in prior studies (e.g., Allam et al., 2017; Martin-Short et al., 2018; Miller, O'Driscoll, et al., 2018; Miller, Roeske, & Benowitz, 2018; Rossi et al., 2006) is also evident in the Vs model (cross-section C, Figure 3). However, in contrast to prior work which focuses on gradients in crustal structure, the results of this study show that the structural gradients across Denali and Hines Creek faults extend through the entire thickness of the upper plate mantle (Figure 3, Figure S4 of Supporting Information S1). While O'Driscoll and Miller (2015) suggested the possibility of a lithospheric thickness change across the Denali fault in one interpretation of their Sp CCP stack (which pre-dated data from the EarthScope Transportable Array), their inferred lithospheric thicknesses significantly differ from the results of this study.

The spatial correlation of the Denali fault (or the Hines Creek plus Northern Foothills Thrust Belt in the central Denali segment), with the southern edge of thicker, higher velocity upper plate lithosphere supports the view that transpressive deformation localizes at gradients in the strength of the upper plate mantle. In particular, the higher velocities in the thicker lithosphere to the north of the deformation zone are consistent with colder temperatures and higher mantle viscosities (e.g., Hirth & Kohlstedt, 2003). The presence of this "backstop" of thicker, more viscous mantle helps to explain the stability of Denali fault curvature, which has remained relatively constant over timescales of ~45 My (Benowitz et al., 2022).

What physical processes explain the localization of transpressive deformation at the edge of the thicker, stronger lithosphere? Numerical models of mantle deformation demonstrate the tendency for strain to localize at the margins of high viscosity mantle (Dayem et al., 2009; Molnar & Dayem, 2010). Localization of mantle deformation may be further enhanced by intrinsic weakness in the mantle of the Denali and Hines Creek fault systems, both of which are reactivated Mesozoic suture zones (Benowitz et al., 2022), by feedback mechanisms in which continued strain reduces mantle strength such as shear heating (Dayem et al., 2009; Regenauer-Lieb et al., 2015; Willis et al., 2019) and/or damage rheologies (Bercovici & Ricard, 2012; Regenauer-Lieb et al., 2015), or by the concentration of upward propagating magmas within the Denali and Hines Creek suture zones (Benowitz et al., 2022).

3.3. Steep Margin to Thick Lithosphere Beneath Northern Alaska

The thickest (>150 km) and highest velocity upper plate lithosphere in Alaska lies beneath the northern Arctic Alaska terrane (Figure 3, cross-sections A-C), which is broadly consistent with evidence for thick lithosphere in this region in prior work (O'Driscoll & Miller, 2015; Martin-Short et al., 2018; Jiang et al., 2018; Feng & Ritzwoller, 2019; Berg et al., 2020; Gama et al., 2021). The maximum velocities in the northern Arctic Alaska terrane mantle (>4.6 km/s, e.g., Figure S3 of Supporting Information S1) are comparable to some cratonic mantles, in that they overlap the globally averaged velocity in the mantle velocity beneath late Proterozoic crust (French & Romanowicz, 2014).

Based on its elevated Vs values and thickness, the lithosphere beneath the portion of the northern Arctic Alaska terrane imaged in this study likely contains relatively cold mantle. While higher Mg# or other variations in bulk chemistry (e.g., Dalton & Faul, 2010; Garber et al., 2018) may also contribute to increasing Vs, the inference of lower mantle temperature is corroborated by low heat flow relative to the rest of Alaska in the northern Arctic Alaska terrane (with the exception of its northernmost tip which is not included in our model) (Batir et al., 2016). The higher viscosities expected for lower temperatures, in combination with distance from subduction in the south, help to explain the low degree of deformation internal to the northern Arctic Alaska terrane shown by geodetic and fault slip data (e.g., Elliott & Freymueller, 2020; Finzel et al., 2015; McConeghy et al., 2022), in contrast to much higher strain rates in the thinner and more deformable lithosphere to the south.

Another striking result is the steep southern margins of some of the highest velocity zones of mantle lithosphere (e.g., cross-section A at ~67.5°N, Figure 3). If these steep margins are old, for example, dating from the time of terrane accretion from the south, which varies from 55 Ma to more than 100 Ma based on different plate accretion models (Clennett et al., 2020; Johnston, 2001; Müller et al., 2019; Plafker & Berg, 1994), then geodynamic models (Currie & van Wijk, 2016) indicate that the mantle lithosphere must be chemically depleted and rheologically strong to have maintained this shape. Alternatively, the steep southern boundary could have been created more recently, perhaps by lithospheric foundering, as suggested at the western margin of the Canadian cratonic mantle at latitudes of 50°N-55°N (Bao et al., 2014). More speculatively, the velocity models may in fact show the presence of foundered fragments of the lithosphere at the southern margin of the northern Arctic-Alaska terrane. The clearest of these potential fragments dips to the south beneath the southern edge of the thick northern lithosphere (at 67°N in cross-section A, Figure 3, and found just north of the Kobuk fault in Figure 2c) and has an along-strike dimension of ~150 km. To explain a similarly near-vertical margin to the Canadian cratonic mantle lithosphere at latitudes of 60°N-65°N (the MacKenzie craton) Estève et al. (2020, 2021) proposed that the Tintina fault cut through the cratonic mantle lithosphere and transported a fragment of the thick lithosphere to the northwest. However, in the case of the northern Arctic Alaska terrane, while the Kobuk fault system lies only ~80 km south of the steep southern face of the thick lithosphere (cross-section A, Figure 3), its (right-lateral) strike-slip displacement is too small (~80 km) (Avé Lallement et al., 1998) to have created such a lithospheric margin. Instead, the strength gradient between the thick lithosphere to the north and the thinner lithosphere to the south may have played a role in the continued localization of deformation (Avé Lallement et al., 1998) on the Kobuk fault system over time.

4. Conclusions

Using data from the Earthscope Transportable Array and other temporary and permanent stations, joint inversion of a Sp common conversion point stack and fundamental mode Rayleigh wave phase velocities from ambient noise and earthquakes have provided a new shear wave velocity model for Alaska. Key features include a well-defined low velocity asthenosphere that extends from the high velocity subducting lithosphere in the south all the way to the Seward Peninsula and to the southern margin of the thick lithosphere beneath the northern Arctic Alaska terrane.

The Denali fault system coincides with a clear northward increase in upper plate lithospheric thickness and velocity. This gradient closely matches the main Denali fault trace except in the central segment of the Denali system where lithospheric thickening correlates better with the Northern Foothills Thrust Belt, the northern limit of Denali-fault-related deformation. This correlation supports the view that transpressive deformation tends to localize at the margins of the thicker, higher-strength lithosphere.

The thick lithosphere beneath the northern Arctic Alaska terrane has velocities comparable to the late Proterozoic cratonic mantle globally, consistent with low temperatures and high viscosity. This gradient in lithospheric strength could have enhanced the localization of deformation on the Kobuk fault system. High-velocity anomalies in the mantle at the foot of the thick northern lithosphere at depths of ∼160 km are consistent with lithospheric foundering playing a role in creating its steep southern face.

This study demonstrates that the Denali fault system, and possibly the Kobuk fault, should be counted among the global tally of continental strike-slip faults that are correlated with offsets in lithospheric thickness, adding evidence for feedback between trans-lithospheric strength heterogeneity and the localization of shallow crustal deformation.

Data Availability Statement

Waveform data employed in this study were obtained from the Incorporated Research Institutions for Seismology (IRIS) Data Management Center (funded through the Seismological Facilities for the Advancement of Geoscience (SAGE) Award of the National Science Foundation under Cooperative Support Agreement EAR-1851048). Data included waveforms from the EarthScope Transportable Array (IRIS Transportable Array, 2003, https://doi.org/10.7914/SN/TA) which was operated by IRIS and supported by the National Science Foundation under Cooperative Agreement EAR-1261681, and other key networks (Alaska Earthquake Center, 1987, https://doi.org/10.7914/SN/AK; Albuquerque Seismological Laboratory/USGS, 2014, https://doi.org/10.7914/SN/IU; Scripps Institution of Oceanography, 1986, https://doi.org/10.7914/SN/II; Albuquerque Seismological Laboratory (ASL)/USGS, 1990, https://doi.org/10.7914/SN/US; Christensen et al., 1999, https://doi.org/10.7914/SN/XE_1999; Song & Christensen, 2004, https://doi.org/10.7914/SN/XR_2004; Hansen & Pavlis, 2005; https://doi.org/10.7914/SN/XZ_2005; Abers & Christensen, 2006, https://doi.org/10.7914/SN/YV_2006; R. Hansen, 2002, https://doi.org/10.7914/SN/YM_2002; Miller, Roeske, & Benowitz, 2018, https://doi.org/10.7914/SN/Z5_2018; and the IM, PN, PP, YE and YG network codes). The shear velocity model and the upper plate lithosphere thicknesses for Alaska created in this study are available through the Brown Digital Repository (https://doi.org/10.26300/dt58-pa32).

Acknowledgments
We are grateful to Lauren Neldner and Ben Davidson for their help in developing the phase velocity maps. We thank Julie Elliott and Jeffrey Benowitz for fault information, and Meghan Miller and an anonymous reviewer for helpful feedback. This research was supported by the US National Science Foundation EarthScope Program (EAR-1829401).

References

Abers, G., & Christensen, D. (2006). Multidisciplinary observations of subduction. [Dataset]. International Federation of Digital Seismograph Networks. https://doi.org/10.7914/SN/YV_2006

Abers, G. A., & Hacker, B. R. (2016). A MATLAB toolbox and Excel workbook for calculating the densities, seismic wave speeds, and major element composition of minerals and rocks at pressure and temperature. *Geochemistry, Geophysics and Geosystems*, *17*(2), 616–624. https://doi.org/10.1002/2015gc006171

Alaska Earthquake Center, Univ. of Alaska Fairbanks. (1987). Alaska regional network [Dataset]. International Federation of Digital Seismograph Networks. https://doi.org/10.7914/SN/AK

Albuquerque Seismological Laboratory (ASL)/USGS. (1990). United States National Seismic Network [Dataset]. International Federation of Digital Seismograph Networks. https://doi.org/10.7914/SN/US

Albuquerque Seismological Laboratory/USGS. (2014). Global Seismograph Network (GSN - IRIS/USGS) [Dataset]. International Federation of Digital Seismograph Networks. https://doi.org/10.7914/SN/IU

Allam, A. A., Schulte-Pelkum, V., Ben-Zion, Y., Tape, C., Ruppert, N., & Ross, Z. E. (2017). Ten-kilometer vertical Moho offset and shallow velocity contrast along the Denali fault zone from double-difference tomography, receiver functions, and fault zone head waves. *Tectonophysics*, *721*, 56–69. https://doi.org/10.1016/j.tecto.2017.09.003

Amante, C., & Eakins, B. W. (2009). ETOPO1 1 Arc-Minute global Relief model: Procedures, data sources and analysis. In NOAA Technical Memorandum NESDIS NGDC-24 [Dataset]. National Geophysical Data Center, NOAA. https://doi.org/10.7289/V5C8276M

Andronikov, A. V., & Mukasa, S. B. (2010). $^{40}Ar/^{39}Ar$ eruption ages and geochemical characteristics of Late Tertiary to Quaternary intraplate and arc-related lavas in interior Alaska. *Lithos*, *115*(1–4), 1–14. https://doi.org/10.1016/j.lithos.2009.11.002

Avé Lallemant, H. G., Gottschalk, R. R., Sisson, V. B., & Oldow, J. S. (1998). Structural analysis of the Kobuk fault zone, north-central Alaska. *Geological Society of America Special Paper*, *324*, 261–268.

Babikoff, J. C., & Dalton, C. A. (2019). Long-period Rayleigh wave phase velocity tomography using USArray. *Geochemistry, Geophysics and Geosystems*, *20*(4), 1990–2006. https://doi.org/10.1029/2018GC008073

Bao, X., Eaton, D., & Guest, B. (2014). Plateau uplift in Western Canada caused by lithospheric delamination along a craton edge. *Nature Geoscience*, *7*(11), 830–833. https://doi.org/10.1038/ngeo2270

Batir, J. F., Blackwell, D. D., & Richards, M. C. (2016). Heat flow and temperature-depth curves throughout Alaska: Finding regions for future geothermal exploration. *Journal of Geophysics and Engineering*, *13*(3), 366–378. https://doi.org/10.1088/1742-2132/13/3/366

Benowitz, J. A., Roeske, S. M., Regan, S. P., Waldien, T. S., Elliott, J. L., & O'Sullivan, P. B. (2022). Large-scale, crustal-block vertical extrusion between the Hines Creek and Denali faults coeval with slip localization on the Denali fault since ca. 45 Ma, Hayes Range, Alaska, USA. *Geosphere*, *18*(3), 1030–1054. https://doi.org/10.1130/ges02466.1

Bercovici, D., & Ricard, Y. (2012). Mechanisms for the generation of plate tectonics by two-phase grain damage and pinning. *Physics of the Earth and Planetary Interiors*, *202–203*, 27–55. https://doi.org/10.1016/j.pepi.2012.05.003

Berg, E. M., Lin, F.-C., Allam, A., Schulte-Pelkum, V., Ward, K. M., & Shen, W. (2020). Shear velocity model of Alaska via joint inversion of Rayleigh wave ellipticity, phase velocities, and receiver functions across the Alaska Transportable Array. *Journal of Geophysical Research: Solid Earth*, *125*(2), 0120100299. https://doi.org/10.1029/2019JB018582

Brennan, P. R., Gilbert, H., & Ridgway, K. D. (2011). Crustal structure across the central Alaska Range: Anatomy of a Mesozoic collisional zone. *Geochemistry, Geophysics, Geosystems*, *12*(4), 1. https://doi.org/10.1029/2011GC003519

Brocher, T. M. (2005). Empirical relations between elastic wavespeeds and density in the Earth's crust. *Bulletin of the Seismological Society of America*, *95*(6), 2081–2092. https://doi.org/10.1785/0120050077

Bürgmann, R., & Dresen, G. (2008). Rheology of the lower crust and upper mantle: Evidence from rock mechanics, geodesy, and field observations. *Annual Review of Earth and Planetary Sciences*, *36*(1), 531–567. https://doi.org/10.1146/annurev.earth.36.031207.124326

Cao, S., & Neubauer, F. (2016). Deep crustal expressions of exhumed strike-slip fault systems: Shear zone initiation on rheological boundaries. *Earth-Science Reviews*, *162*, 155–176. https://doi.org/10.1016/j.earscirev.2016.09.010

Chen, L., Zheng, T., & Xu, W. (2006). A thinned lithospheric image of the Tanlu fault zone, eastern China: Constructed from wave equation based receiver function migration. *Journal of Geophysical Research*, *111*(B9), B09312. https://doi.org/10.1029/2005jb003974

Christensen, D., Hansen, R., & Abers, G. (1999). Broadband experiment across the Alaska range [Dataset]. International Federation of Digital Seismograph Networks. https://doi.org/10.7914/SN/XE_1999

Clennett, E. J., Sigloch, K., Mihalynuk, M. G., Seton, M., Henderson, M. A., & Hosseini, K. (2020). A quantitative tomotectonic plate reconstruction of Western North America and the eastern Pacific basin. *Geochemistry, Geophysics, Geosystems*, *20*(8), e2020GC009117. https://doi.org/10.1029/2020GC009117

Colpron, M., & Nelson, J. L. (2011). A Digital Atlas of terranes for the northern Cordillera [Dataset]. Accessed online from Yukon Geological Survey. Retrieved from www.geology.gov.yk.ca

Colpron, M., Nelson, J. L., & Murphy, D. C. (2007). Northern Cordilleran terranes and their interactions through time. *Geological Society of America Today*, *17*(4–5), 4–10. https://doi.org/10.1130/gsat01704-5a.1

Currie, C. A., & van Wijk, J. (2016). How craton margins are preserved: Insights from geodynamic models. *Journal of Geodynamics*, *100*, 144–158. https://doi.org/10.1016/j.jog.2016.03.015

Dalton, C. A., & Faul, U. H. (2010). The oceanic and cratonic upper mantle: Clues from joint interpretation of global velocity and attenuation models. *Lithos*, *120*(1–2), 160–172. https://doi.org/10.1016/j.lithos.2010.08.020

Daly, K., Abers, G. A., Mann, M. E., Roecker, S. R., & Christensen, D. H. (2021). Subduction of an oceanic plateau across Southcentral Alaska: High-resolution seismicity. *Journal of Geophysical Research: Solid Earth*, *126*(11), e2021JB022809. https://doi.org/10.1029/2021jb022809c

Dayem, K. E., Houseman, G. A., & Molnar, P. (2009). Localization of shear along a lithospheric strength discontinuity: Application of a continuous deformation model to the boundary between Tibet and the Tarim Basin. *Tectonics*, *28*(3). https://doi.org/10.1029/2008tc002264

Eilon, Z., Fischer, K. M., & Dalton, C. A. (2018). An adaptive Bayesian inversion for upper-mantle structure using surface waves and scattered body waves. *Geophysical Journal International*, *214*(1), 232–253. https://doi.org/10.1093/gji/ggy137

Ekström, G., Abers, G. A., & Webb, S. C. (2009). Determination of surface-wave phase velocities across USArray from noise and Aki's spectral formulation. *Geophysical Research Letters*, *36*(18), 5–9. https://doi.org/10.1029/2009GL039131

Elliott, J., & Freymueller, J. T. (2020). A block model of present-day kinematics of Alaska and Western Canada. *Journal of Geophysical Research: Solid Earth*, *125*(7), e2019JB018378. https://doi.org/10.1029/2019JB018378

Estève, C., Audet, P., Schaeffer, A. J., Schutt, D. L., Aster, R. C., & Cubley, J. F. (2020). Seismic evidence for craton chiseling and displacement of lithospheric mantle by the Tintina fault in the northern Canadian Cordillera. *Geology*, *48*(11), 1120–1125. https://doi.org/10.1130/G47688.1

Estève, C., Gosselin, J. M., Audet, P., Schaeffer, A. J., Schutt, D. L., & Aster, R. C. (2021). Surface-wave tomography of the northern Canadian Cordillera using earthquake Rayleigh wave group velocities. *Journal of Geophysical Research: Solid Earth*, *126*(8), e2021JB021960. https://doi.org/10.1029/2021JB021960

Feng, L., & Ritzwoller, M. H. (2019). A 3-D shear velocity model of the crust and upper-most mantle beneath Alaska including apparent radial anisotropy. *Journal of Geophysical Research: Solid Earth*, *124*(10), 10468–10497. https://doi.org/10.1029/2019jb018122

Fichtner, A., Saygin, E., Taymaz, T., Cupillard, P., Capdeville, Y., & Trampert, J. (2013). The deep structure of the North Anatolian fault zone. *Earth and Planetary Science Letters*, *373*, 109–117. https://doi.org/10.1016/j.epsl.2013.04.027

Finzel, E. S., Flesch, L. M., Ridgway, K. D., Holt, W. E., & Ghosh, A. (2015). Surface motions and intraplate continental deformation in Alaska driven by mantle flow. *Geophysical Research Letters*, *42*(11), 4350–4358. https://doi.org/10.1002/2015GL063987

Ford, H. A., Fischer, K. M., & Lekic, V. (2014). Localized shear in the deep lithosphere beneath the San Andreas fault system. *Geology*, *42*(4), 295–298. https://doi.org/10.1130/g35128.1

French, S. W., & Romanowicz, B. A. (2014). Whole-mantle radially anisotropic shear velocity structure from spectral-element waveform tomography. *Geophysical Journal International*, *199*(3), 1303–1327. https://doi.org/10.1093/gji/ggu334

Gama, I., Fischer, K. M., Eilon, Z., Krueger, H. E., Dalton, C. A., & Flesch, L. M. (2021). Shear-wave velocity structure beneath Alaska from a Bayesian joint inversion of Sp receiver functions and Rayleigh wave phase velocities. *Earth and Planetary Science Letters*, *560*, 116785. https://doi.org/10.1016/j.epsl.2021.116785

Gama, I., Fischer, K. M., & Hua, J. (2022). Mapping the lithosphere and asthenosphere beneath Alaska with Sp converted waves. *Geochemistry, Geophysics, Geosystems*, *23*, e2022GC010517. https://doi.org/10.1029/2022GC010517

Garber, J. M., Maurya, S., Hernandez, J. A., Duncan, M. S., Zeng, L., Zhang, H. L., et al. (2018). Multidisciplinary constraints on the abundance of diamond and eclogite in the cratonic lithosphere. *Geochemistry, Geophysics, Geosystems*, *19*(7), 2062–2086. https://doi.org/10.1029/2018gc007534

Haney, M. M., Ward, K. M., Tsai, V. C., & Schmandt, B. (2020). Bulk structure of the crust and upper mantle beneath Alaska from an approximate Rayleigh-wave dispersion formula. *Seismological Society of America*, *91*(6), 3064–3075. https://doi.org/10.1785/0220200162

Hansen, R. (2002). Denali fault aftershocks RAMP [Dataset]. International Federation of Digital Seismograph Networks. https://doi.org/10.7914/SN/YM_2002

Hansen, R., & Pavlis, G. (2005). Collaborative research: St. Elias Erosion/tectonics Project [Dataset]. International Federation of Digital Seismograph Networks. https://doi.org/10.7914/SN/XZ_2005

Hansen, S. M., & Schmandt, B. (2017). P and S wave receiver function imaging of subduction with scattering kernels. *Geochemistry, Geophysics, Geosystems*, *18*(12), 4487–4502. https://doi.org/10.1002/2017GC007120

Hastings, W. K. (1970). Monte Carlo sampling methods using Markov chains and their applications. *Biometrika*, *57*(1), 97–109. https://doi.org/10.1093/biomet/57.1.97

Hayes, G. P., Moore, G. L., Portner, D. E., Hearne, M., Flamme, H., Furtney, M., & Smoczyk, G. M. (2018). Slab2, a comprehensive subduction zone geometry model. *Science*, *362*(6410), 58–61. https://doi.org/10.1126/science.aat4723

Hirth, G., & Kohlstedt, D. L. (2003). Rheology of the upper mantle and the mantle wedge: A view from the experimentalists. *Geophysical Monograph-American Geophysical Union*, *138*, 83–106. https://doi.org/10.1029/138gm06

Hua, J., Fischer, K. M., Mancinelli, N. J., & Bao, T. (2020). Imaging with pre-stack migration based on Sp scattering kernels. *Geophysical Journal International*, *220*(1), 428–449. https://doi.org/10.1093/gji/ggz459

Hua, J., Fischer, K. M., & Savage, M. K. (2018). The lithosphere–asthenosphere boundary beneath the South Island of New Zealand. *Earth and Planetary Science Letters*, *484*, 92–102. https://doi.org/10.1016/j.epsl.2017.12.011

Hua, J., Fischer, K. M., Wu, M., & Blom, N. A. (2020). New approaches to multifrequency Sp stacking tested in the Anatolian region. *Journal of Geophysical Research: Solid Earth*, *125*(11), e2020JB020313. https://doi.org/10.1029/2020JB020313

IRIS Transportable Array. (2003). USArray Transportable Array. [Dataset]. International Federation of Digital Seismograph Networks. https://doi.org/10.7914/SN/TA

Jadamec, M. A., Billen, M. I., & Roeske, S. M. (2013). Three-dimensional numerical models of flat slab subduction and the Denali fault driving deformation in south-central Alaska. *Earth and Planetary Science Letters*, *376*, 29–42. https://doi.org/10.1016/j.epsl.2013.06.009

Jiang, C., Schmandt, B., Ward, K. M., Lin, F. C., & Worthington, L. L. (2018). Upper mantle seismic structure of Alaska from Rayleigh and S wave tomography. *Geophysical Research Letters*, *45*(19), 10350–10359. https://doi.org/10.1029/2018GL079406

Johnston, S. T. (2001). The Great Alaskan terrane wreck: Reconciliation of paleomagnetic and geological data in the northern Cordillera. *Earth and Planetary Science Letters*, *193*(3–4), 259–272. https://doi.org/10.1016/s0012-821x(01)00516-7

Keith, C. M., & Crampin, S. (1977). Seismic body waves in anisotropic media: Synthetic seismograms. *Geophysical Journal of the Royal Astronomical Society*, *49*(1), 225–243. https://doi.org/10.1111/j.1365-246x.1977.tb03710.x

Kennett, B. L. N., Engdahl, E. R., & Buland, R. (1995). Constraints on seismic velocities in the Earth from travel times. *Geophysical Journal International*, *122*(1), 108–124. https://doi.org/10.1111/j.1365-246x.1995.tb03540.x

Lekic, V., & Fischer, K. M. (2017). Interpreting spatially stacked Sp receiver functions. *Geophysical Journal International*, *210*(2), 874–886. https://doi.org/10.1093/gji/ggx206

Lekic, V., French, S. W., & Fischer, K. M. (2011). Lithospheric thinning beneath rifted regions of Southern California. *Science*, *334*(6057), 783–787. https://doi.org/10.1126/science.1208898

Mann, M. E., Abers, G. A., Daly, K., & Christensen, D. H. (2022). Subduction of an oceanic plateau across Southcentral Alaska: Scattered-wave imaging. *Journal of Geophysical Research: Solid Earth*, *127*(1), e2021JB022697. https://doi.org/10.1029/2021jb022697

Martin-Short, R., Allen, R., Bastow, I. D., Porritt, R. W., & Miller, M. S. (2018). Seismic imaging of the Alaska subduction zone: Implications for slab geometry and volcanism. *Geochemistry, Geophysics and Geosystems*, *19*(11), 4541–4560. https://doi.org/10.1029/2018GC007962

Masters, G., Woodhouse, J. H., & Freeman, G. (2011). Mineos v1.0.2. Computational infrastructure for geodynamics. [Software]. Retrieved from https://geodynamics.org/cig/software/mineos/

McConeghy, J., Flesch, L., & Elliott, J. (2022). Investigating the effect of mantle flow and viscosity structure on surface velocities in Alaska using 3-D geodynamic models. *Journal of Geophysical Research: Solid Earth*, *127*(10), e2022JB02470. https://doi.org/10.1029/2022JB024704

Miller, M. S., & Becker, T. W. (2014). Reactivated lithospheric-scale discontinuities localize dynamic uplift of the Moroccan Atlas. *Mountains: Geology*, *42*(1), 35–38. https://doi.org/10.1130/G34959.1

Miller, M. S., O'Driscoll, L. J., Porritt, R. W., & Roeske, S. M. (2018). Multiscale crustal architecture of Alaska inferred from P receiver functions. *Lithosphere*, *10*(2), 267–278. https://doi.org/10.1130/L701.1

Miller, M. S., Roeske, S. M., & Benowitz, J. A. (2018). A four-dimensional view of deformation in the Eastern Alaska Range - Where did the slip on the Denali fault go? [Dataset]. International Federation of Digital Seismograph Networks. https://doi.org/10.7914/SN/Z5_2018

Molnar, P., & Dayem, K. E. (2010). Major intracontinental strike-slip faults and contrasts in lithospheric strength. *Geosphere*, *6*(4), 444–467. https://doi.org/10.1130/ges00519.1

Mukasa, S. B., Andronikov, A. V., & Hall, C. M. (2007). The $^{40}Ar/^{39}Ar$ chronology and eruption rates of Cenozoic volcanism in the eastern Bering Sea Volcanic Province, Alaska. *Journal of Geophysical Research*, *112*(B6), B06207. https://doi.org/10.1029/2006JB004452

Müller, R. D., Zahirovic, S., Williams, S. E., Cannon, J., Seton, M., Bower, D. J., et al. (2019). A global plate model including litho-spheric deformation along major rifts and orogens since the Triassic. *Tectonics*, *38*(6), 1884–1907. https://doi.org/10.1029/2018TC005462

Nayak, A., Eberhart-Phillips, D., Ruppert, N. A., Fang, H., Moore, M. M., Tape, C., et al. (2020). 3D seismic velocity models for Alaska from joint tomographic inversion of body-wave and surface-wave data. *Seismological Research Letters*, *91*(6), 3106–3119. https://doi.org/10.1785/0220200214

Norris, R. J., & Toy, V. G. (2014). Continental transforms: A view from the Alpine Fault. *Journal of Structural Geology*, *64*, 3–31. https://doi.org/10.1016/j.jsg.2014.03.003

O'Driscoll, L. J., & Miller, M. S. (2015). Lithospheric discontinuity structure in Alaska, thickness variations determined by Sp receiver functions. *Tectonics*, *34*(4), 694–714. https://doi.org/10.1002/2014TC003669

Plafker, G., & Berg, H. C. (1994). In G. Plafker, & H. C. Berg (Eds.), (pp. 989–1021). Geological Society of America The Geology of North America series v. G-1.Overview of the geology and tectonic evolution of Alaska*The Geology of Alaska*.

Regan, S. P., Benowitz, J. A., & Holland, M. E. (2020). A plutonic brother from another magma mother: Disproving the Eocene Foraker-McGonagall pluton piercing point and implications for long-term slip on the Denali fault. *Terra Nova*, *32*(1), 66–74. https://doi.org/10.1111/ter.12437

Regenauer-Lieb, K., Rosenbaum, G., Lyakhovsky, V., Liu, J., Weinberg, R., Segev, A., & Weinstein, Y. (2015). Melt instabilities in an intraplate lithosphere and implications for volcanism in the Harrat Ash-Shaam volcanic field (NW Arabia). *Journal of Geophysical Research: Solid Earth*, *120*(3), 1543–1558. https://doi.org/10.1002/2014JB011403

Rossi, G., Abers, G. A., Rondenay, S., & Christensen, D. H. (2006). Unusual mantle Poisson's ratio, subduction, and crustal structure in central Alaska. *Journal of Geophysical Research*, *111*(B9), B09311. https://doi.org/10.1029/2005jb003956

Scripps Institution of Oceanography. (1986). Global Seismograph network - IRIS/IDA [Dataset]. International Federation of Digital Seismograph Networks. https://doi.org/10.7914/SN/II

Song, X., & Christensen, D. (2004). CSEDI: Observational and theoretical constraints on the structure and rotation of the inner core [Dataset]. International Federation of Digital Seismograph Networks. https://doi.org/10.7914/SN/XR_2004

Teyssier, C., & Tikoff, B. (1998). Strike-slip partitioned transpression of the San Andreas Fault system: A lithospheric-scale approach. *Geological Society, London, Special Publications*, *135*(1), 143–158. https://doi.org/10.1144/gsl.sp.1998.135.01.10

Titus, S. J., Medaris, L. G., Jr., Wang, H. F., & Tikoff, B. (2007). Continuation of the San Andreas Fault system into the upper mantle: Evidence from spinel peridotite xenoliths in the Coyote lake basalt, central California. *Tectonophysics*, *429*(1–2), 1–20. https://doi.org/10.1016/j.tecto.2006.07.004

Vauchez, A., Tommasi, A., & Mainprice, D. (2012). Faults (shear zones) in the Earth's mantle. *Tectonophysics*, *558–559*, 1–27. https://doi.org/10.1016/j.tecto.2012.06.006

Veenstra, E., Christensen, D. H., Abers, G. A., & Ferris, A. (2006). Crustal thickness variation in south-central Alaska. *Geology*, *34*(9), 781–784. https://doi.org/10.1130/g22615.1

Ward, K. M. (2015). Ambient noise tomography across the southern Alaskan Cordillera. *Geophysical Research Letters*, *42*(9), 3218–3227. https://doi.org/10.1002/2015GL063613

Willis, K., Houseman, G. A., Evans, L., Wright, T., & Hooper, A. (2019). Strain localization by shear heating and the development of lithospheric shear zones. *Tectonophysics*, *764*, 62–76. https://doi.org/10.1016/j.tecto.2019.05.010

Wittlinger, G., Tapponnier, P., Poupinet, G., Mei, J., Danian, S., Herquel, G., & Masson, F. (1998). Tomographic evidence for localized lithospheric shear along the Altyn Tagh Fault. *Science*, *282*(5386), 74–76. https://doi.org/10.1126/science.282.5386.74

Yang, X., & Gao, H. (2020). Segmentation of the Aleutian-Alaska subduction zone revealed by full-wave ambient noise tomography: Implications for the along-strike variation of volcanism. *Journal of Geophysical Research: Solid Earth*, *125*(11), e2020JB019677. https://doi.org/10.1029/2020JB019677

Zhang, Y., Li, A., & Hu, H. (2019). Crustal structure in Alaska from receiver function analysis. *Geophysical Research Letters*, *46*(3), 1284–1292. https://doi.org/10.1029/2018GL081011

References From the Supporting Information

Jin, G., & Gaherty, J. B. (2015). Surface wave phase-velocity tomography based on multichannel cross-correlation. *Geophysical Journal International*, *201*(3), 1383–1398. https://doi.org/10.1093/gji/ggv079

Lin, F.-C., Ritzwoller, M. H., & Snieder, R. (2009). Eikonal tomography: Surface wave tomography by phase front tracking across a regional broadband seismic array. *Geophysical Journal International*, *177*(3), 1091–1110. https://doi.org/10.1111/j.1365-246x.2009.04105.x